

See discussions, stats, and author profiles for this publication at: <https://www.researchgate.net/publication/231645454>

Growth and Surface Structure of Zinc Oxide Layers on a Pd(111) Surface

ARTICLE in THE JOURNAL OF PHYSICAL CHEMISTRY C · AUGUST 2010

Impact Factor: 4.77 · DOI: 10.1021/jp104620n

CITATIONS

40

READS

56

7 AUTHORS, INCLUDING:



Giovanni Barcaro

Italian National Research Council

106 PUBLICATIONS 1,571 CITATIONS

SEE PROFILE



Alessandro Fortunelli

Italian National Research Council

210 PUBLICATIONS 3,945 CITATIONS

SEE PROFILE



Frederik Weber

AVL LIST GMBH

6 PUBLICATIONS 54 CITATIONS

SEE PROFILE

Growth and Surface Structure of Zinc Oxide Layers on a Pd(111) Surface

G. Weirum,^{†,‡} G. Barcaro,[§] A. Fortunelli,[§] F. Weber,[‡] R. Schennach,[‡] S. Surnev,^{*,†} and F. P. Netzer[†]*Institute of Physics, Karl-Franzens University Graz, A-8010 Graz, Austria, Institute of Solid State Physics, Graz University of Technology, A-8010 Graz, Austria, and Molecular Modeling Laboratory, IPCF-CNR, I-56124 Pisa, Italy**Received: May 20, 2010; Revised Manuscript Received: July 30, 2010*

The growth and geometric structure of ultrathin zinc oxide films on Pd(111) has been studied by scanning tunneling microscopy, low-energy electron diffraction, and density functional theory calculations. For sub-monolayer coverages, depending on the oxygen pressure, two well-ordered zinc oxide phases with (4×4) and (6×6) coincidence structures form, which are attributed to H-terminated Zn_6O_5 and graphite-like Zn_6O_6 layers, respectively. The (6×6) phase exhibits a pronounced oxygen pressure dependence: at low $p(\text{O}_2)$ a well-ordered (6×6) two-dimensional array of O vacancies develops, yielding a layer with a formal $\text{Zn}_{25}\text{O}_{24}$ stoichiometry, while at high $p(\text{O}_2)$ the Zn_6O_6 monolayer transforms into bilayer islands. For oxide coverages up to 4 monolayers the graphite-like Zn_6O_6 structure is thermodynamically the most stable phase over a large range of oxygen chemical potentials, before it converges to the bulk-type wurtzite structure. Under oxygen-poor conditions a compressed overlayer of Zn adatoms can be stabilized on top of the Zn_6O_6 structure.

1. Introduction

Polar oxide surfaces (i.e., with a finite dipole moment perpendicular to the surface) are of fundamental scientific interest because of their inherent instability in bulk samples. For such surfaces to occur, the surface dipole must be quenched by reduction of the charges of the surface layer, which is realized either by reconstruction or by adsorption of foreign molecules.^{1,2} Notable examples are the Zn- and O-terminated polar basal faces of zinc oxide (ZnO), which are referred to as $(0001)\text{-Zn}$ and $(000\bar{1})\text{-O}$. The structure stabilization mechanism of these two polar surfaces has been extensively investigated mainly on macroscopic bulk crystals. The current picture evolving for the $(0001)\text{-Zn}$ -terminated surface implies that it is stabilized by nanoscaled triangular islands of a magic size, in which about 25% of the Zn ions is missing.^{3,4} Density functional theory (DFT) calculations have suggested that this mechanism should be stable over a large range of oxygen and hydrogen chemical potentials.⁵ Recent atomic force microscopy (AFM) data have shown that at elevated temperatures an additional stabilization channel is possible for the $(0001)\text{-Zn}$ -terminated surface, involving faceting via the formation of regular step arrays.⁶ For the $(000\bar{1})\text{-O}$ -terminated surface no consensus model on the stabilization mechanism has been reached up to now. This surface is very reactive and easily dissociates water, which results in a H-stabilized unreconstructed (1×1) surface.⁷ This is also corroborated by ab initio calculations, which have predicted that over a wide range of temperatures and pressures the hydrogenated surface is the most stable one.⁸ Removal of the hydrogen results in reconstructed surfaces, which have been reported to be of either (1×3) -⁹ or more recently of $(\sqrt{3} \times \sqrt{3})R30^\circ$ type.¹⁰ No structural models for these two reconstructions are available yet.

For nanosize oxide objects, such as ultrathin films with a thickness of only a few atomic layers, new depolarization mechanisms may become effective, which originate from the stabilizing role of the support and/or from the ability of finite systems to sustain a nonzero polarization along the polar axis.² In the specific case of ZnO, it has been theoretically predicted that unsupported thin films adopt a nonpolar graphite-like structure.^{11,12} This result has been confirmed by a recent X-ray diffraction (XRD) and scanning tunneling microscopy (STM) study of ZnO films grown on a Ag(111) surface,¹³ which has demonstrated that the graphite-like structure is maintained for the first two atomic layers and then transforms gradually into the bulk wurtzite structure upon increasing the film thickness.

In this work we investigate the growth mechanism and the surface structure of zinc oxide layers deposited on a Pd(111) surface. The choice of the Pd surface as a support has been motivated by the catalytic relevance of the Pd/ZnO system, in particular for the steam reforming of methanol.^{14–16} Here, the investigated zinc oxide/Pd(111) nanolayers can be regarded as a model system, which is reversed with respect to the technologically employed one, an approach that has been proven as particularly useful when the focus of the study is on the physical and chemical properties of the oxide–metal interface.^{17–19} The oxide–metal interface has been demonstrated to have a strong influence on the termination of ZnO surfaces.^{20,21} By using a combination of STM measurements and DFT calculations, we show that the structure and stoichiometry of zinc oxide overlayers depend strongly on the oxygen pressure and the zinc coverage. At sub-monolayer coverages two planar oxide phases with (4×4) and (6×6) unit cells coexist on the Pd(111) surface, whose structures have been rationalized in the DFT analysis as H-terminated Zn_6O_5 and graphite-like Zn_6O_6 coincidence layers, respectively. The latter structure exhibits a pronounced oxygen pressure dependence: at low $p(\text{O}_2)$ a well-ordered (6×6) -array of O vacancies develops, yielding a layer with a formal $\text{Zn}_{25}\text{O}_{24}$ stoichiometry, while at high $p(\text{O}_2)$ Zn_6O_6 bilayer islands become more favorable. For coverages above 1

* To whom correspondence should be addressed. Tel.: +43 316 380 8553. Fax: +43 316 380 9816. E-mail: svetlozar.surnev@uni-graz.at.

[†] Karl-Franzens University Graz.

[‡] Graz University of Technology.

[§] IPCF-CNR.

monolayer the Zn_6O_6 graphite-like phase is thermodynamically the most stable structure over a large range of oxygen chemical potentials and persists up to 4 monolayers. At low oxygen pressures a layer of Zn adatoms may become stabilized on top of the Zn_6O_6 structure.

2. Experimental and Theoretical Details

All experiments have been carried out in an ultrahigh-vacuum (UHV) chamber operating at a base pressure of 1×10^{-10} mbar. The chamber is equipped with STM, low-energy electron diffraction (LEED), and facilities for crystal cleaning and physical vapor deposition. The STM measurements have been performed in a constant current mode with an Omicron micro-STM at room temperature.²² The tips have been prepared by electrochemical etching of a 0.3 mm tungsten wire and by in situ cleaning in UHV by electron bombardment. Clean Pd(111) surfaces have been obtained by cycles of 1.5 kV Ar^+ -ion sputtering and annealing to 1000 K. The annealing cycles have been carried out first in UHV followed by a heating to 800 K in an oxygen atmosphere of 5×10^{-7} mbar to remove carbon. Finally the sample has been flashed to 1000 K in UHV to desorb the residual oxygen. The cleanliness of the surface has been controlled by LEED and STM.

The zinc oxide films have been prepared by depositing metallic zinc (99.98%, Goodfellow) at room temperature (300 K) onto the Pd(111) surface, which has been subjected to oxidation either during (reactive evaporation) or after the Zn deposition (postoxidation). For the Zn deposition a Knudsen cell with a resistively heated boron–nitride crucible has been used. The Zn deposition rate has been calibrated by a quartz microbalance and STM²³ and controlled by precise temperature adjustment of the crucible. The zinc oxide coverages are given in monolayers, with 1 monolayer corresponding to the deposited amount of Zn atoms as determined by the quartz microbalance and referred to the density of the Pd(111) surface (1.52×10^{15} atoms·cm⁻²). Oxygen has been dosed via a leak valve at pressures varying between 5×10^{-8} and 5×10^{-6} mbar, with the sample held at 550 K. Typically the postoxidation technique has been used for sub-monolayer oxide coverages, whereas the reactive evaporation method has been preferred for coverages >1 monolayer in order to avoid possible alloying at the Pd interface.²³ In a final step, the sample has been annealed at 550 K in oxygen atmosphere for 5 min to achieve better ordered oxide films.

Spin-unpolarized DFT calculations were performed using the PWSCF (plane-wave self-consistent field) computational code,²⁴ employing ultrasoft pseudopotentials²⁵ and the Perdew–Burke–Ernzerhof (PBE) exchange–correlation functional.²⁶ Values of 30 and 150 Ry were used as the energy cutoff for the selection of the plane wave basis set for the description of the wave function and the electronic density, respectively. A Gaussian smearing technique with a broadening of the one-particle levels of 0.03 eV was applied. Hexagonal unit cells were adopted for simulating (6×6) and (4×4) phases. The metallic slabs have been built using a first-neighbor metal–metal distance equal to the equilibrium value predicted in fcc palladium (2.80 Å) by our DFT/PBE approach. A minimum empty space of about 10 Å has been inserted along the direction perpendicular to the surface to prevent dipole interaction between replicated cells. For the (6×6) compact phase, two Pd layers (each containing 36 metal atoms) have been used for the metallic slab in relaxation calculations and four Pd layers in single-point calculations to simulate STM images. Sampling of the first Brillouin zone was achieved via a $(2,2,1)$ k -point

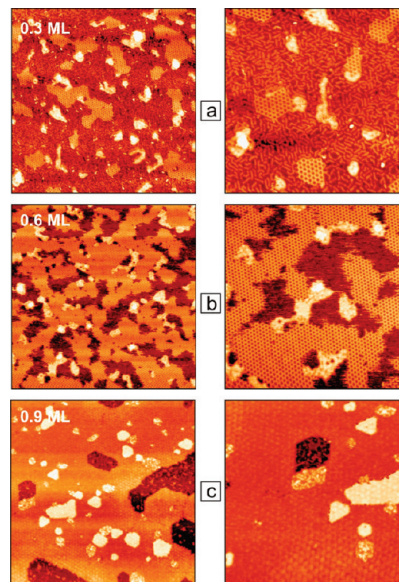


Figure 1. STM images of sub-monolayer zinc oxide films. Images in the left (right) panels are $1000 \text{ Å} \times 1000 \text{ Å}$ ($500 \text{ Å} \times 500 \text{ Å}$) large: (a) 0.3 monolayer (+1 V, 0.4 nA; +0.7 V, 0.4 nA); (b) 0.6 monolayer (+1 V, 0.4 nA; +1 V, 1 nA); (c) 0.9 monolayer (+1 V, 0.4 nA; +1 V, 1 nA).

grid, sufficiently accurate for this large unit cell. For the (4×4) phase, the metallic slab was described using four Pd layers (each containing 16 metal atoms) and a $(4,4,1)$ k -point grid. STM images were simulated using the Tersoff–Hamann approach²⁷ at a bias of +1.0 V. The simulated STM images were recorded at a distance of 2.0–2.2 Å above the topmost atomic layer. A value of 10^{-4} – 10^{-5} au for the isosurface contour was used in all cases.

The Car–Parrinello (CP) simulations were performed using the same code.²⁴ The time step was set to 25 au, the electron mass to 3500 au, a CP run consisted of 500 minimization steps, 200 MD steps starting with null velocities at 300 K, and a variable number of production MD steps at the chosen temperature for a total simulation time between 3 and 5 ps using a nose thermostat for the kinetic energy of the electronic wave function. Thermodynamic calculations in section 3.3 always neglect phonon contributions of the extended phases.

3. Results and Discussion

In section 3.1 we introduce first the zinc oxide film growth at a fixed oxygen pressure of 5×10^{-7} mbar and describe the various structures encountered as a function of the oxide coverage. The evolution of the zinc oxide film morphology and structure as a function of the oxygen pressure is then presented in section 3.2. Finally, in section 3.3 we discuss the experimental results in the light of DFT-derived structure models.

3.1. Zinc Oxide Growth at $p(\text{O}_2) = 5 \times 10^{-7}$ mbar. Figure 1 summarizes the growth morphology of zinc oxide layers in the sub-monolayer coverage regime, as imaged by STM. At low oxide coverages (e.g., 0.3 monolayer, Figure 1a) two types of flat zinc oxide islands coexist on the Pd(111) surface: larger ones with an open network structure and an apparent height of 1.4 Å and smaller compact, more irregular islands with a height of 1.8 Å. In between, the Pd(111) surface is covered by wormlike clusters, which are one atomic row wide and have an average length of about 20 Å. Increasing the oxide coverage to 0.6 monolayer (Figure 1b) causes mainly the growth of the network structure islands, which become the dominant phase.

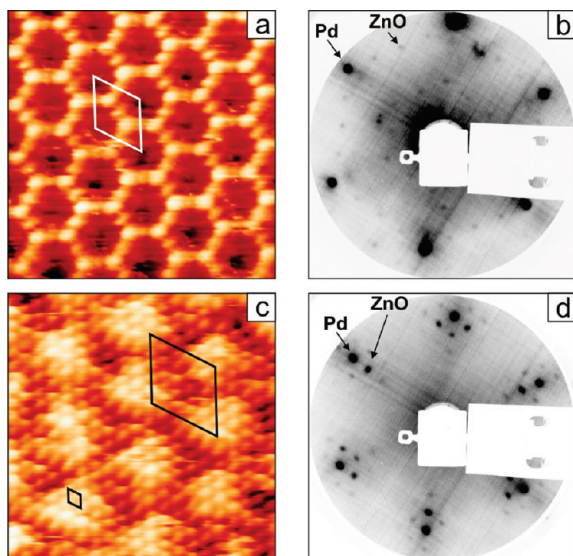


Figure 2. (a) High-resolution STM image of the (4×4) phase ($65 \text{ \AA} \times 65 \text{ \AA}$; +10 mV, 3 nA), (b) corresponding (4×4) LEED pattern (electron energy, 66.9 eV), (c) high-resolution STM image of the (6×6) phase ($50 \text{ \AA} \times 50 \text{ \AA}$; +100 mV, 2 nA), and (d) corresponding (6×6) LEED pattern (electron energy, 71.6 eV).

Repetitive STM scans over the same area were found to result in the formation of the wormlike clusters from the network structure islands, suggesting that the clusters are decomposition products of the oxide islands induced by the STM tip. As the oxide coverage approaches 1 monolayer (Figure 1c), the film structure changes dramatically: the network structure islands are completely replaced by the compact islands, which form an almost closed wetting layer with few second-layer islands on top. The $(500 \text{ \AA} \times 500 \text{ \AA})$ STM image of the 0.9 monolayer surface (Figure 1c, right) shows a hexagonal structure with a large-scale periodicity, which is indicative of a Moiré pattern, as discussed below. The monolayer structures reported in Figure 1 clearly differ from the $p(2 \times 1)$ structure characteristic of the PdZn(111) surface alloy, which forms after the deposition of similar amounts of metallic Zn in UHV onto the clean Pd(111) surface.²³ Moreover, X-ray-excited Auger electron spectra (Supporting Information) taken from the oxidized Zn layers exhibit a Zn $L_3M_{45}M_{45}$ peak located at a kinetic energy of 991 eV, which is compatible with ZnO, whereas this transition on the ZnPd alloy surface is observed at a kinetic energy of 994 eV.²³

Details of the atomic structure of the monolayer phases are displayed in Figure 2. Figure 2a shows a high-resolution STM image of the network structure islands at 0.6 monolayer, which exhibit a honeycomb-type hexagonal unit cell (indicated in the image) with a length of 11 \AA , corresponding to 4 times the lattice constant of the Pd(111) surface, in agreement with the $p(4 \times 4)$ LEED pattern in Figure 2b. The latter is very sensitive to electron beam damage, vanishing after a few seconds of beam exposure. The honeycomb hexagons of the $p(4 \times 4)$ structure consist of 12 maxima, half of which are located at the corners and appear with a brighter contrast. The atomic-resolved STM image in Figure 2c has been taken from the compact phase, which is dominant at 0.9 monolayer. It exhibits a hexagonal structure with a lattice constant of $b_{\text{ox}} = 3.2 \text{ \AA}$ (unit cell indicated with a small rhomb in Figure 2c), which is identical with the in-plane lattice parameter (3.25 \AA) of the ZnO(0001) surfaces. In addition, a Moiré-type pattern with a periodicity of 16.5 \AA can be recognized in the image (indicated by the larger unit cell). The latter corresponds to 6 times the Pd(111) lattice

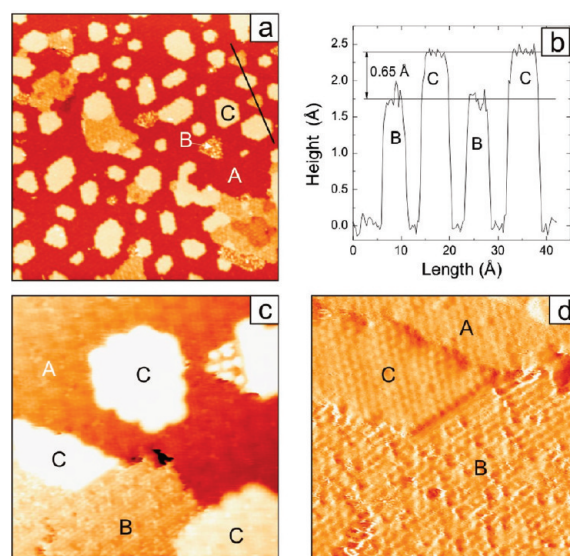


Figure 3. (a) Large-scale STM image of 1.5 monolayers of zinc oxide ($1000 \text{ \AA} \times 1000 \text{ \AA}$; +1 V, 0.4 nA). The first (6×6) monolayer is indicated by A, and the second layer islands are indicated by B and C; (b) the height profile is taken along the line drawn in a, showing the height difference between the B and C islands of the second layer; (c) the image shows the high-resolution image of this surface ($200 \text{ \AA} \times 200 \text{ \AA}$; +300 mV, 2 nA); (d) the differentiated image shows the A–C surfaces with atomic resolution ($100 \text{ \AA} \times 100 \text{ \AA}$; +300 mV, 2 nA).

constant or to 5 times the b_{ox} value and thus represents a coincidence lattice. The contrast modulation within the coincidence cell originates from the different registry of Zn and O atoms with respect to the Pd substrate atoms. These findings are also reflected in the corresponding LEED pattern (Figure 2d), which shows satellite spots arranged in hexagons around the Pd diffraction spots, with a side length of $1/6$ the separation between the Pd spots. The formation of the satellite diffraction spots can be explained in terms of multiple scattering processes between the Pd substrate and the coincidence oxide overlayer lattice and is in line with the observed Moiré pattern in the STM image of Figure 2c. This coincidence zinc oxide structure will be designated as (6×6) in the following. A similar (8×8) coincidence structure has been recently reported for the growth of ZnO layers on a Ag(111) surface, which exhibit a nonpolar graphite-like structure.¹³ Our DFT calculations (see section 3.3) also indicate that the (6×6) monolayer adopts a similar planar geometry.

At 1.5 monolayers the (6×6) layer (labeled A in Figure 3a) is completed and second layer islands of triangular (labeled B) and hexagonal (labeled C) shapes have grown on top. A line profile across a few second layer islands (Figure 3b) reveals that the hexagonal islands exhibit an apparent height of $\sim 2.4 \text{ \AA}$ with respect to the (6×6) layer and are higher than the triangular islands by about 0.6 \AA . This height difference is almost equal to the shorter interplane distance (0.61 \AA) between Zn and O (0001) planes of the wurtzite ZnO structure. Moreover, it has been reported by Dulub et al.^{3,4} that single crystal ZnO(0001)–Zn-terminated surfaces are typically covered by triangular islands and pits, whereas the ZnO(0001)–O-terminated surfaces are characterized by hexagonal terraces and double steps. Thus, at a first sight, it is tempting to assign the B and C islands in Figure 3a to different terminations of the ZnO(0001) surface. The atomic structures of the B- and C-island surfaces are detailed in the STM images in Figure 3c,d. Both second layer B and C islands exhibit a hexagonal structure with the lattice constant of the (6×6) layer underneath (A).

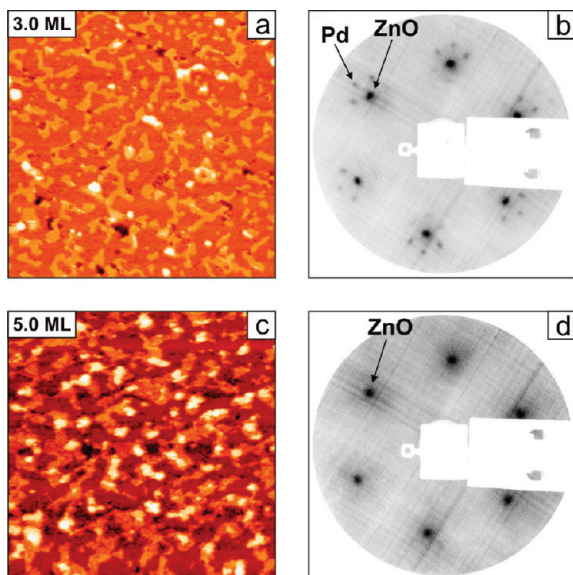


Figure 4. Structure and morphology of ZnO films up to 5 monolayers. STM images are displayed in the left panels; the corresponding LEED patterns, in the right panels: (a) STM image of 3.0 monolayers ($1000 \text{ \AA} \times 1000 \text{ \AA}$; +1 V, 0.4 nA); (b) corresponding LEED pattern (70.2 eV); (c) STM image of 5.0 monolayers ($1000 \text{ \AA} \times 1000 \text{ \AA}$; +1 V, 0.4 nA); (d) corresponding LEED pattern (70.2 eV).

However, whereas the A and C layers have a similar appearance in STM (a Moiré pattern can be also observed on the C islands) and display atomically flat surfaces, the B layer is somewhat rougher due to the presence of numerous irregular protrusions (see the spikes on the B islands in the line profile of Figure 3b), which are presumably due to adsorbates. Later, in section 3.3, the C islands will be associated in our DFT analysis with a second graphite-like ZnO layer and a possible structure model of the B-type islands will be proposed.

The layer-by-layer growth mode of ZnO films on Pd(111) persists also for oxide coverages of up to 5 monolayers, as exemplified in the topographic STM images of Figure 4 (left panel). The oxide surface consists of a flat layer, which is covered by islands of the B and C type with their characteristic apparent heights of 1.8 and 2.4 Å, respectively. No atomically resolved STM images could be obtained at these oxide coverages, but the LEED patterns in the right panels of Figure 4 reveal a good structural order. Both the Pd and the satellite diffraction spots are attenuated, which is in line with the observed layer-by-layer growth mechanism of the ZnO films. Thicker oxide films, with coverages above 5 monolayers, display typically rough morphologies, characteristic of polycrystalline film growth. Presumably, the temperature of oxide preparation (550 K) was too low to provide sufficient mass transport and thus to obtain a better structural order. This temperature was limited by the onset of the ZnO decomposition at $\sim 570\text{--}580 \text{ K}$, as observed by thermal desorption spectroscopy (not shown).

3.2. Oxygen Pressure Dependence of the Zinc Oxide Growth. Figure 5 shows a set of STM images, illustrating the evolution of the structure of sub-monolayer (0.6–0.7 monolayer) zinc oxide coverages on Pd(111) with the oxygen pressure. The oxide layers have been prepared by the postoxidation technique; i.e., following the Zn metal deposition at 300 K, the oxygen pressure has been varied during the annealing step between 5×10^{-8} and 5×10^{-6} mbar. Prior to the oxidation step, ZnPd alloy islands form, which exhibit a dendritic shape and a $p(2 \times 1)$ structure.²³ First, at a low oxygen pressure of 5×10^{-8} mbar the Pd(111) surface is covered by a mixture of islands with the

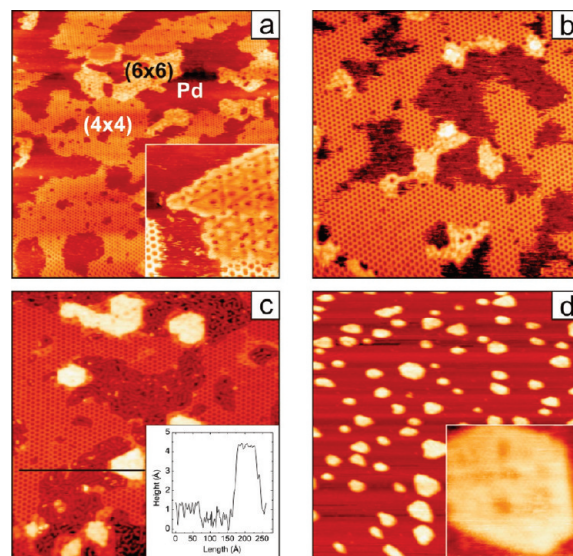


Figure 5. STM images of sub-monolayer ($\sim 0.6\text{--}0.7$ monolayer) zinc oxide coverages prepared at different oxygen pressures: (a) 5×10^{-8} mbar O_2 ($1000 \text{ \AA} \times 1000 \text{ \AA}$; +1 V, 0.4 nA) [inset ($200 \text{ \AA} \times 200 \text{ \AA}$; +30 mV, 1.5 nA)]; (b) 1×10^{-7} mbar O_2 ($500 \text{ \AA} \times 500 \text{ \AA}$; +1 V, 1 nA); (c) 1×10^{-6} mbar O_2 ($500 \text{ \AA} \times 500 \text{ \AA}$; +1 V, 1 nA) [inset: line profile taken along the line (black), indicated on the image]; (d) 5×10^{-6} mbar O_2 ($1500 \text{ \AA} \times 1500 \text{ \AA}$; +1 V, 0.4 nA) [inset: bilayer island surface ($200 \text{ \AA} \times 200 \text{ \AA}$; +0.5 V, 1 nA)].

(4×4) and (6×6) structure and bare Pd patches in between (Figure 5a). A more detailed look (see inset of Figure 5a) reveals that the (6×6) Moiré pattern appears differently than on the surface prepared at $p(\text{O}_2) = 5 \times 10^{-7}$ mbar (see Figure 2c), displaying an array of depressions. A similar Moiré pattern has been reported for reduced $\text{CeO}_{2-x}(\text{111})$ overlayers on a $\text{Rh}(\text{111})$ surface²⁸ and ascribed to the formation of an ordered array of oxygen vacancies promoted by the lattice mismatch at the oxide–metal interface. As discussed in more detail in section 3.3 the depressions of the (6×6) islands can be also associated with missing oxygen atoms in the zinc oxide layer. Increasing the oxygen pressure to 1×10^{-7} mbar causes a reduction of the area of the (6×6) islands with respect to that of the (4×4) islands (Figure 5b). The depressions in the Moiré pattern of the (6×6) islands have disappeared (not shown), most likely as a result of the annihilation of the oxygen vacancies under the more O-rich conditions. Dramatic structure changes occur for oxygen pressures exceeding 1×10^{-6} mbar, as seen in the STM image of Figure 5c: the single layer (6×6) islands become replaced by smaller but higher islands, whereas the (4×4) islands remain unaffected. The apparent height of the higher islands is $4.3 \pm 0.2 \text{ \AA}$ (see line profile in the inset of Figure 5c) and is equal to that of the C islands with respect to the Pd(111) surface, which can be thus considered as bilayer islands. Oxidation at 5×10^{-6} mbar of O_2 results in the full conversion also of the (4×4) islands into the bilayer islands (Figure 5d), which now exhibit predominantly hexagonal shapes with alternating edge lengths. The surface of the bilayer islands is atomically flat, as seen in the high-resolution STM image in the inset of Figure 5d, which displays a hexagonal lattice with a constant of 3.3 Å, i.e., virtually identical to that of the (6×6) structure. Thus, the dewetting of the single layer into bilayer (6×6) islands signals an improved energetic stability of the latter at higher oxygen chemical potentials, as discussed below in section 3.3.

The effect of the oxygen pressure on the structure of thicker zinc oxide films (>1 monolayer) is illustrated in Figure 6 for

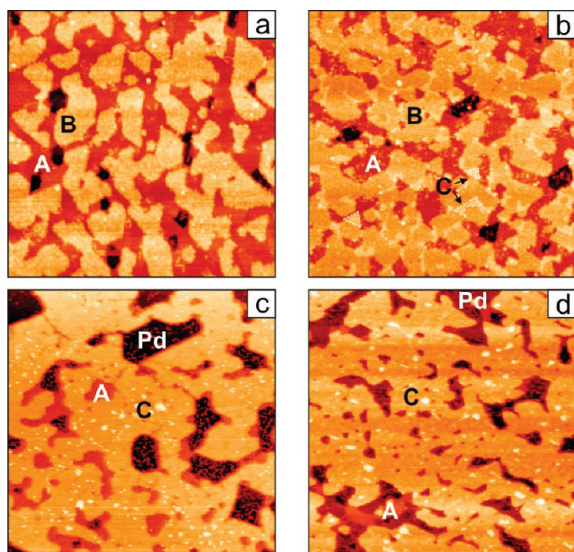


Figure 6. STM images ($1000 \text{ \AA} \times 1000 \text{ \AA}$) of 1.8 monolayers of zinc oxide films prepared at different oxygen pressures: (a) 5×10^{-8} mbar O_2 (+1 V, 0.4 nA); (b) 1×10^{-7} mbar O_2 (+1 V, 0.4 nA). Some of the C islands are highlighted on the image with a white dotted line; (c) 1×10^{-6} mbar O_2 (+1 V, 0.4 nA); (d) 1×10^{-5} mbar O_2 (+1 V, 0.4 nA).

an oxide coverage of 1.8 monolayers. In this case the oxygen pressure cited corresponds to that during the reactive evaporation of the Zn atoms. The STM image in Figure 6a shows that oxidation in 5×10^{-8} mbar of oxygen yields an oxide surface consisting of the first (6×6) monolayer (A) and the B-type islands in the second layer with their typical apparent height of about 1.7 \AA with respect to the A layer. Small uncovered patches of the bare Pd surface can be seen as well with a dark contrast. Increasing the oxygen pressure to 1×10^{-7} mbar (Figure 6b) causes the appearance of small triangular C-type (bilayer) islands, indicated with the arrows, with a relative apparent height of $\sim 2.4 \text{ \AA}$. As already mentioned, at an oxygen pressure of 5×10^{-7} mbar (Figure 3), the B- and C-type islands coexist on the surface, with the C islands dominating. This is also seen here upon increasing the oxygen pressure, and for $p(\text{O}_2) \geq 1 \times 10^{-6}$ mbar only the C islands are present in the second layer (Figure 6c,d). In addition, there is a tendency of the first (6×6) monolayer (A) to dewet at the expense of forming a bilayer, as visible from the significant area reduction of the uncovered A patches and the concomitant increase of the bare Pd surface. This behavior is analogous to the dewetting of the sub-monolayer zinc oxide islands and their transformation into bilayer islands at elevated oxygen pressures, as reported above.

3.3. DFT Analysis. We start by considering the structure of the (6×6) compact phase. Due to the similarity of the coincidence lattice shown in Figure 2c with Figure 2d of ref 13, a nonpolar graphitic-like structure was assumed and subjected to DF local relaxation. The relaxed structural model and the simulated STM image are shown in Figure 7a,b and are in excellent agreement with the experimental images (Figure 2c). Note that O atoms are imaged as bright spots, as discussed in ref 29 for the $\text{ZnO}/\text{Ag}(111)$ system. Growing further graphitic-like ZnO monolayers (up to 4) on top of the first layer leads to stable local minima, with an interesting behavior of the structural properties. In fact, the increase in average height (the z -direction, orthogonal to the surface) of the oxide atoms in the 1, 2, 3, and 4 monolayers systems is 2.54 , 2.56 , 2.54 , and 2.54 \AA for Zn atoms and 2.75 , 2.45 , 2.59 , and 2.59 \AA for O atoms, respectively. These values compare well with the

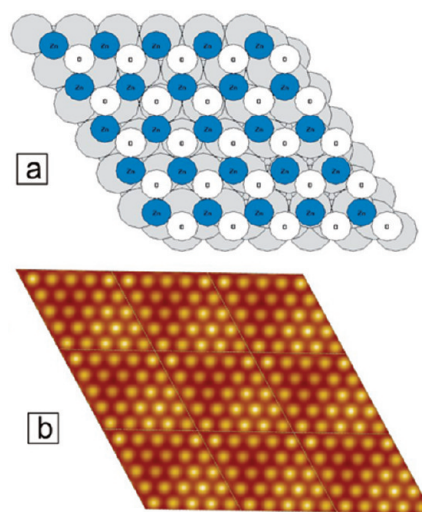


Figure 7. (a) Unit cell of the ZnO -(6×6) compact phase. Pd atoms are shown in light gray, whereas O atoms are in white and Zn atoms in light blue (dark gray); (b) simulated STM image of 9 unit cells of the (6×6) phase at +1.0 V.

experimental apparent height of the second layer (C) of around 2.4 \AA . The square root deviation of the average heights is small in the first monolayer, 0.07 and 0.08 \AA for Zn and O atoms, respectively, but rapidly increases with the number of layers, reaching its maximum of 0.24 (0.29) \AA in the interfacial layer, 0.22 (0.31) \AA in the second layer, 0.24 (0.28) in the third layer, and 0.10 (0.23) \AA in the topmost layer for Zn (O) atoms for the 4 monolayers system, witnessing the tendency of the graphitic-like configuration to transform into a wurtzite-like structure.

The open network (4×4) structure present at sub-monolayer coverage poses an apparent problem which challenges this structural assignment. A graphitic-like structure should in fact be even more favorable than a polar wurtzite-like termination as the coverage tends to zero, but it is difficult to fit such a structure into the STM pattern (peak-to-peak distance) of Figure 2a. First, we tried several structural models with different stoichiometry and checked that even at sub-monolayer coverage O atoms rather than Zn atoms are imaged as bright spots in the simulated STM images. We then constructed a pattern of O atoms matching the experimental STM image of Figure 2a and inserted a variable number of Zn atoms in proper interatomic positions, ending up with the structural model depicted in Figure 8a, having stoichiometry Zn_6O_5 . This model presents two problems. First, in the simulated STM image three-coordinated O atoms (darker spots) are clearly distinguishable from two-coordinated O atoms (brighter spots), as shown in Figure 8b. Second, this structure indeed represents a local minimum but, via a minor heating (simulated via Car–Parrinello runs), collapses into a graphitic-like one, shown in Figure 8c, in which Zn and O atoms are almost coplanar and which is lower in energy by $0.3 \text{ eV}/(\text{unit cell})$. However, the corresponding simulated STM image (shown in Figure 8d) does not bear much resemblance with the experimental data. A different depolarization mechanism must therefore be active, that along the lines of ref 7, we hypothesize being termination by hydrogen atoms. We therefore set up the model of Figure 8e, in which all the O atoms are saturated with H. This structure not only is now a local minimum but is also stable to heating to 300 K for 1 ns (via Car–Parrinello simulations). Figure 8f shows the simulated STM pattern, which is now in good agreement with Figure 2a. It should be stressed in this connection that complete saturation is energetically favorable: the $\text{Zn}_6(\text{OH})_5$ structure has a Gibbs

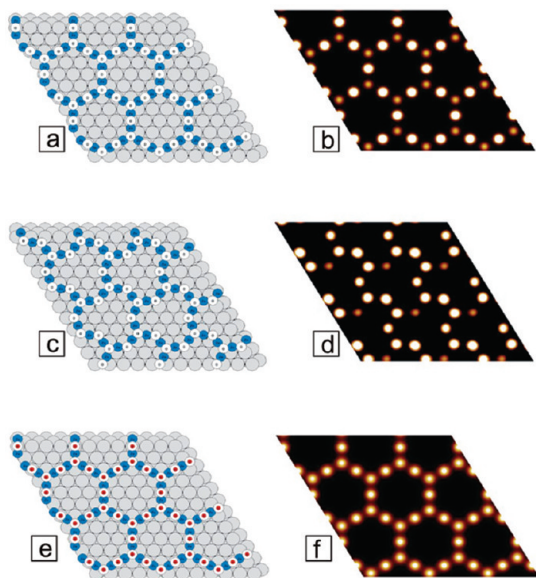


Figure 8. Structural models and simulated STM images at +1.0 V of the ZnO-(4×4) phase: (a, b) ZnO₅ polar phase; (c, d) ZnO₅ planar phase; (e, f) ZnO₅H₃ phase. Color coding as in Figure 7, plus H atoms in red.

free energy (G) lower by 0.35 eV with respect to dissociation of H atoms to give $[\text{Zn}_6\text{O}_5\text{H}_3 + \text{H}_2]$ at $T = 550$ K and $p(\text{H}_2) = 5 \times 10^{-7}$ mbar. Note also that the most stable orientation of the H atoms is perpendicular to the surface, but the H atoms bound to 2-fold coordinated oxygens are rather floppy and can oscillate from one side of the hexagon to the other quite easily. We believe that this is reflected in the experimental STM images as a weaker signal from these oxygens, even though this is not visible in the theoretical STM images (Figure 8f), simulated at 0 K. The hypothesis that the (4 × 4) phase is stabilized by H termination also explains why repetitive STM scans destroy the network structure islands and transform them into wormlike strings, and the fact that the $p(4 \times 4)$ LEED pattern is very sensitive to electron beam damage, as discussed in section 3.1.

Also the (6 × 6) compact phase can be stabilized by H termination, and this should be taken into account in a thermodynamic comparison of the two phases. The Gibbs free energy of the reaction



is −0.12 eV at $p(\text{O}_2) = 5 \times 10^{-7}$ mbar and −0.14 eV at $p(\text{O}_2) = 5 \times 10^{-8}$ mbar, respectively, where the H₂ molecule is assumed to reside in the gas phase. However, in real experimental conditions H atoms do not come from the gas phase but are provided by the Pd(111) surface or the Pd bulk, so that the chemical potential of H adsorbed on the Pd surface or dissolved into the Pd support should be used in these thermodynamic considerations. In addition, kinetic effects will obviously play an important role in the (6 × 6) vs (4 × 4) competition. As it stands, the (4 × 4) phase seems favored by increasing pressure, which is not fully in tune with the observations reported in section 3.2.

It is clear anyway that the (4 × 4) phase cannot sustain coverages higher than 3/8 monolayer, so that it gradually fills up its voids and transforms into the (6 × 6) phase. The latter phase can easily give rise to a multilayer system, as described above, explaining for example the regions denoted as C in Figure

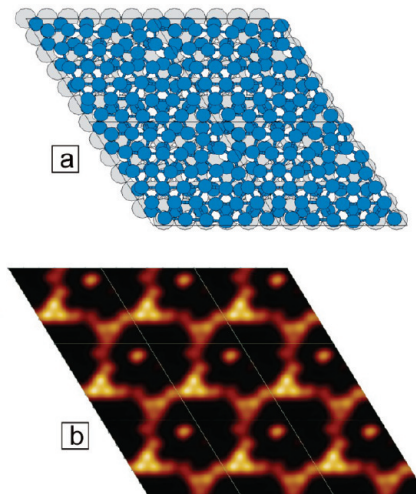
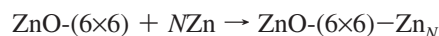


Figure 9. Structural model (a) and STM image (b) simulated at +1.0 V of the 38-atoms Zn overlayer grown on the compact ZnO-(6×6) phase. Color coding as in Figure 7.

3 (bilayer) or the hexagonal regions in Figure 4 (multilayer), as the simulated STM images (not shown) are very similar to Figure 7b. The regions denoted as B in Figure 3 are apparently different. On the basis of the hints discussed in section 3.1, we assumed that the B islands in Figure 3 and the triangular features in Figure 4 corresponded to Zn-terminated ZnO islands. We thus constructed models in which a (6×6)-ZnO monolayer was covered with a variable number of Zn atoms and optimized the resulting models via a combination of Car–Parrinello simulations and local energy relaxations. This Zn overlayer turns out to be very stable, and one can add up to 38 Zn atoms per (6 × 6) unit cell, always increasing the differential binding energy. The Gibbs free energy corresponding to the formation of the Zn overlayer is calculated via the following reaction:



as a function of N (the number of Zn atoms in the overlayer). The chemical potential of Zn (μ_{Zn}) was approximated as the binding energy of hcp metallic zinc, predicted by our DFT approach. The Gibbs free energy of the above reaction has a minimum at $N = 38$ with value $\Delta G = -2.56$ eV, vs a ΔG of −2.11 eV at $N = 36$ and −1.91 eV at $N = 40$. The model of the 38-atoms Zn overlayer is depicted in Figure 9a, whereas the simulated STM image is shown in Figure 9b. Some protruding Zn atoms give rise to irregular bright spots. It should be taken into account, however, that a Zn-terminated phase can only be stabilized by the presence of absorbates, which are the likely sources of the bright features exhibited by the B islands in Figure 3. From a thermodynamic point of view, a regular ZnO bilayer is clearly much favored with respect to a Zn-terminated phase.

We then briefly discuss the behavior of the ZnO/Pd(111) system with oxygen pressure. At $p(\text{O}_2) = 5 \times 10^{-8}$ mbar, the (6 × 6) phase is imaged differently with respect to higher O₂ pressure and displays an array of depressions (inset of Figure 5a), hypothesized in section 3.2 to be oxygen vacancies. A model based on this hypothesis was set up and is shown in Figure 10a. The corresponding STM image, shown in Figure 10b, matches reasonably well the experimental pattern. However, our calculations predict that the formation of vacancy

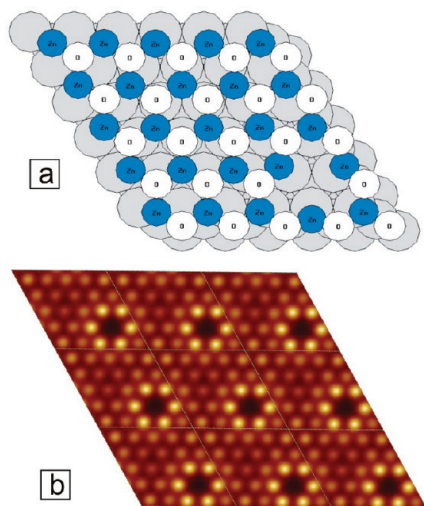
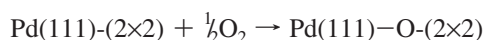


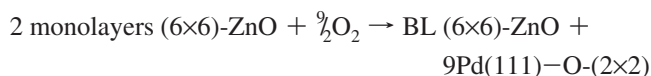
Figure 10. Structural model (a) and STM image (b) simulated at +1.0 V of a model in which an oxygen vacancy is created inside the compact ZnO-(6×6) phase. Color coding as in Figure 7.

should not be favored at $p(\text{O}_2) = 5 \times 10^{-8}$ mbar and $T = 550$ K, as experimentally observed, but only at a temperature of $T = 800$ K.

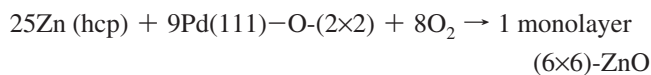
Finally, the dewetting of a single layer into bilayer islands observed in Figure 5c,d, instead, can be explained as the competition of O binding to the Zn with respect to the Pd(111) surface. It is known, in fact, that a (2 × 2) chemisorbed phase can be formed on Pd(111), according to the following scheme:



with $\Delta G = -0.55$ eV at $T = 550$ K and $p(\text{O}_2) = 5 \times 10^{-7}$ mbar according to our DFT approach. The reaction



where BL indicates the bilayer ZnO islands, has a ΔG of -4.26 eV in these conditions and is thus thermodynamically favored. Clearly, this is possible if the Zn coverage is substantially less than 1 monolayer. The reaction



is in fact thermodynamically favored by -2.98 eV in the same conditions. A disagreement with experimental data lies in the fact that our DFT approach predicts that this transformation is favored up to $T = 800$ K. We note that, however, the inaccuracy in theoretical prediction concerning the dependence upon oxygen pressure of the ZnO growth is probably connected to the overestimation of O-binding with the chosen xc-functional and ultrasoft pseudopotential.

4. Conclusions

We have investigated the growth and surface structure of zinc oxide layers with a coverage of up to 5 monolayers on a Pd(111) surface. Our STM results, supported by DFT calculations, have shown that a nonpolar graphite-like (6×6)-ZnO₆ layer is

thermodynamically the most stable structure over a large range of oxygen pressures and Zn coverages. The fact that the same oxide structure also forms on other metal substrates, such as, e.g., Ag(111),¹³ suggests that layer confinement and/or polarity cancellation effects rather than interactions across the oxide–metal interface are the reason for the stabilization of this peculiar phase. At sub-monolayer coverages the (6×6)-ZnO₆ layer transforms at O-poor conditions into a Zn₂₅O₂₄ layer containing a (6 × 6) array of oxygen vacancies, whereas at O-rich conditions bilayer (6×6)-ZnO₆ islands, coexisting with bare Pd areas covered by chemisorbed oxygen, become energetically more favorable. An intriguing structure model has been proposed in the DFT analysis for another sub-monolayer phase, exhibiting a (4 × 4) open network structure, which involves termination of an oxygen layer with hydrogen atoms, yielding a formal Zn₆(OH)₅ stoichiometry.

Acknowledgment. Financial support was provided by the Austrian Science Funds (FWF) within Project P19198 and by the ERC Advanced Grant SEPON (Search for Emergent Phenomena in Oxide Nanostructures). DFT calculations were performed at CASPUR Supercomputing Center (Rome, Italy) within the “Competitive HPC Grant 2009” E-MOON project.

Supporting Information Available: Figure S1, showing Mg K α -excited Zn L₂₃M₄₅M₄₅ Auger transition of a 0.6 monolayer zinc oxide film on Pd(111) prepared at an oxygen pressure of 5×10^{-7} mbar. This material is available free of charge via the Internet at <http://pubs.acs.org>.

References and Notes

- (1) Noguera, C. *J. Phys.: Condens. Matter* **2000**, *12*, R367.
- (2) Goniakowski, J.; Finocchi, F.; Noguera, C. *Rep. Prog. Phys.* **2008**, *71*, 016501.
- (3) Dulub, O.; Boatner, L. A.; Diebold, U. *Surf. Sci.* **2002**, *519*, 201.
- (4) Dulub, O.; Diebold, U.; Kresse, G. *Phys. Rev. Lett.* **2003**, *90*, 016102.
- (5) Kresse, G.; Dulub, O.; Diebold, U. *Phys. Rev. B* **2003**, *68*, 245409.
- (6) Ostendorf, F.; Torbrügge, S.; Reichling, M. *Phys. Rev. B* **2008**, *77*, 041405 (R).
- (7) Kunat, M.; Girol, S. G.; Becker, Th.; Burghaus, U.; Wöll, Ch. *Phys. Rev. B* **2002**, *66*, 081402 (R).
- (8) Meyer, B.; Marx, D. *Phys. Rev. B* **2003**, *67*, 035403.
- (9) Kunat, M.; Girol, S. G.; Burghaus, U.; Wöll, Ch. *J. Phys. Chem. B* **2003**, *107*, 14350.
- (10) King, S. T.; Parihar, S. S.; Pradhan, K.; Johnson-Steigleman, H. T.; Lyman, P. F. *Surf. Sci. Lett.* **2008**, *602*, L131.
- (11) Claeysens, F.; Freeman, C. L.; Allan, N. L.; Sun, Y.; Ashfold, M. N. R.; Harding, J. H. *J. Mater. Chem.* **2005**, *15*, 139.
- (12) Claeysens, F.; Freeman, C. L.; Allan, N. L.; Harding, J. H. *Phys. Rev. Lett.* **2006**, *96*, 066102.
- (13) Tusche, C.; Meyerheim, H. L.; Kirschner, J. *Phys. Rev. Lett.* **2007**, *99*, 026102.
- (14) Iwasa, N.; Yamamoto, O.; Akazawa, T.; Ohya, S.; Takezawa, N. *J. Chem. Soc., Chem. Commun.* **1991**, 1322.
- (15) Iwasa, N.; Kudo, S.; Takahashi, H.; Masuda, S.; Takezawa, N. *Catal. Lett.* **1993**, *19*, 211.
- (16) Iwasa, N.; Masuda, S.; Ogawa, N.; Takezawa, T. *Appl. Catal., A* **1995**, *125*, 145.
- (17) Leisenberger, F. P.; Surnev, S.; Koller, G.; Ramsey, M. G.; Netzer, F. P. *Surf. Sci.* **2000**, *444*, 211.
- (18) Surnev, S.; Sock, M.; Kresse, G.; Andersen, J. N.; Ramsey, M. G.; Netzer, F. P. *J. Phys. Chem. B* **2003**, *107*, 4777.
- (19) Schoiswohl, S.; Eck, S.; Ramsey, M. G.; Andersen, J. N.; Surnev, S.; Netzer, F. P. *Surf. Sci.* **2005**, *580*, 122.
- (20) Zaoui, A. *Phys. Rev. B* **2004**, *69*, 115403.
- (21) Sakaguchi, N.; Suzuki, Y.; Watanabe, K.; Iwama, S.; Watanabe, S.; Ichinose, H. *Philos. Mag.* **2008**, *88*, 1493.
- (22) Kraft, J.; Ramsey, M. G.; Netzer, F. P. *Phys. Rev. B* **1997**, *55*, 5384.
- (23) Weirum, G.; Kratzer, M.; Koch, H. P.; Tamtögl, A.; Killmann, J.; Bako, I.; Winter, A.; Surnev, S.; Netzer, F. P.; Schennach, R. *J. Phys. Chem. C* **2009**, *113*, 9788.

(24) Giannozzi, P.; Baroni, S.; Bonini, N.; Calandra, M.; Car, R.; Cavazzoni, C.; Ceresoli, D.; Chiarotti, G. L.; Cococcioni, M.; Dabo, I.; Dal Corso, A.; de Gironcoli, S.; Fabris, S.; Fratesi, G.; Gebauer, R.; Gerstmann, U.; Gougoussis, C.; Kokalj, A.; Lazzeri, M.; Martin-Samos, L.; Marzari, N.; Mauri, F.; Mazzarello, R.; Paolini, S.; Pasquarello, A.; Paulatto, L.; Sbraccia, C.; Scandolo, S.; Sclauzero, G.; Seitsonen, A. P.; Smogunov, A.; Umari, P.; Wentzcovitch, R. M. *J. Phys.: Condens. Matter* **2009**, *21*, 395502.

(25) Vanderbilt, D. *Phys. Rev. B* **1990**, *41*, 7892.

(26) Perdew, J. P.; Burke, K.; Ernzerhof, M. *Phys. Rev. Lett.* **1996**, *77*, 3865.

(27) Tersoff, J.; Hamann, D. R. *Phys. Rev. Lett.* **1983**, *50*, 1998.

(28) Castellarin-Cudia, C.; Surnev, S.; Schneider, G.; Podlucky, R.; Ramsey, M. G.; Netzer, F. P. *Surf. Sci. Lett.* **2004**, *554*, L120.

(29) Barcaro, G.; Thomas, I. O.; Fortunelli, A. *J. Chem. Phys.* **2010**, *132*, 124703.

JP104620N